

# On the Heating of the Solar Corona and the Acceleration of the Low-Speed Solar Wind by Acoustic Waves Generated in the Corona

Takeru Ken Suzuki

stakeru@th.nao.ac.jp

*Division of Theoretical Astrophysics, National Astronomical Observatory, 2-21-1 Osawa, Mitaka, Tokyo, Japan 181-8588; Department of Astronomy, Faculty of Science, University of Tokyo, 7-3-1 Hongo, Bunkyo-ku, Tokyo, Japan 113-0033*

## ABSTRACT

We investigate possibilities of solar coronal heating by acoustic waves generated not at the photosphere but in the corona, aiming at heating in the mid- to low-latitude corona where the low-speed wind is expected to come from. Acoustic waves of period  $\tau \sim 100$ s are triggered by chromospheric reconnection, one model of small scale magnetic reconnection events recently proposed by Sturrock. These waves having a finite amplitude eventually form shocks to shape sawtooth waves (N-waves), and directly heat the surrounding corona by dissipation of their wave energy. Outward propagation of the N-waves is treated based on the weak shock theory, so that the heating rate can be evaluated consistently with physical properties of the background coronal plasma without setting a dissipation length in an ad hoc manner. We construct coronal structures from the upper chromosphere to the outside of 1AU for various inputs of the acoustic waves having a range of energy flux of  $F_{w,0} = (1 - 20) \times 10^5 \text{erg cm}^{-2} \text{s}^{-1}$  and a period of  $\tau = 60 - 300$ s. The heating by the N-wave dissipation effectively works in the inner corona and we find that the waves of  $F_{w,0} \geq 2 \times 10^5 \text{erg cm}^{-2} \text{s}^{-1}$  and  $\tau \geq 60$ s could maintain peak coronal temperature,  $T_{\text{max}} > 10^6 \text{K}$ . The model could also reproduce the density profile observed in the streamer region. However, due to its short dissipation length, the location of  $T_{\text{max}}$  is closer to the surface than the observation, and the resultant flow velocity of the solar wind is lower than the observed profile of the low-speed wind. The cooperations with other heating and acceleration sources with the larger dissipation length are inevitable to reproduce the real solar corona.

*Subject headings:* Sun: corona — solar wind — waves

## 1. Introduction

The heating of the solar is been still poorly understood, and it is one of the most challenging but interesting questions to be solved in astrophysics. The origin of energy that heats the corona is generally believed to lurk in the turbulent convective motions beneath the photosphere. A certain fraction of the kinetic energy of those turbulent motions is carried up to the corona in the shape of non-thermal energy, such as magnetic or wave energy, and thermalization of such energy in the corona results in the heating of the surrounding plasma. Granule motions of the surface convection simply expect wave generation at the photospheric level. Possibilities of coronal heating by those waves have been investigated by many researchers (Osterbrock 1961; Ulmschneider 1971; McWhirter, Thonemann, & Wilson 1975 ). To date, among various modes of waves, although an Alfvén wave has widely taken up as a convincing candidate in coronal heating and acceleration of the high-speed wind in the polar coronal holes through the ion-cyclotron damping mechanism (e.g. Cranmer, Field, & Kohl 1999; Hollweg 1999), acoustic waves have not been regarded as a major heating source of the corona because of their dissipative character. Acoustic waves with a finite amplitude inevitably steepen their wave fronts to form shocks when they travel. They are strongly damped through upward propagation in the chromosphere, consequently the only 0.01% of the initial wave energy could reach the corona (Stein & Schwartz 1972; hereafter SS). A role of acoustic waves in solar coronal heating has been buried in oblivion for a long time.

However, recent observations of dynamical structures of the solar corona (see Aschwanden, Poland, & Rabin 2001 for recent review) highlight a role of acoustic waves generated not at the photosphere but in the corona. A large number of flares and flare-like events (e.g. Tsuneta et al.1992; Tsuneta 1996) have been observed by various telescopes until today (e.g. Nishio et al.1997; see Bastian, Benz, & Gary 1998 for review) in a wide range of energy from  $\sim 10^{24}$ erg to  $\sim 10^{32}$ erg, and they are statistically argued in terms of supply of bulk energy to heat the global corona. Recent measurements of EUV frequency distribution,  $\frac{dN}{dE}(E) \propto E^{-\alpha}$ , of flare-like events gives a steeper power-law index ( $\alpha = 2.3 - 2.6$  by Krucker & Benz 1998;  $\alpha = 2.0 - 2.6$  by Parnell & Jupp 2000) on the lower energy side ( $E = 10^{24} - 10^{25}$ erg). This fact makes us infer that small-scale flare-like events, such as nano-flares, might be sufficient (Hudson 1991) for the required energy budget ( $\gtrsim 10^{5.5}$ erg cm $^{-2}$ s $^{-1}$ ; Withbroe & Noyes 1977). Several models taking into account such small-scale events have been introduced (Sturrock 1999; hereafter S99; Sturrock, Roald, & Wolfson 2000; Roald, Sturrock, & Wolfson 2000; hereafter RSW; Tarbell, Ryutova, & Covington 1999; Sakai et al. 2000; Furusawa & Sakai 2000). Among these models, S99 proposed a model of chromospheric magnetic reconnection. In this model, a flux tube, newly formed as a result of reconnection events, oscillates vertically to excite acoustic waves in the corona. RSW further showed based on a simple kinetic

model that this process possibly liberates the sufficient energy in the corona with the correct relevant parameters. A different mechanism also predicts generation of acoustic waves in the corona. For example, spicules in the open magnetic field region effectively transports energy of random motions at the photosphere into the corona and produce longitudinal (acoustic) waves there (Hollweg 1992; Kudoh & Shibata 1999). Thus, acoustic waves are supposed to be generated constantly in the corona by various dynamical processes. Such acoustic waves could heat the surrounding corona directly, unlike acoustic waves created at the photospheric level. They are expected to heat the inner corona effectively by the shock dissipation. Therefore, density at the coronal base might be large enough to create dense wind flow observed as the streamer in the mid- to low-latitude region, which is believed to be connected to the low-speed solar wind (Habbal et al. 1997). Acoustic waves might become one of relevant processes working in the region generating the low-speed wind of which mechanisms have been poorly elucidated.

In the above models introducing production of acoustic waves in the corona, the authors concentrated on the amount of kinetic (wave) energy released in the corona. However, heating of coronal gas is accomplished by thermalization of wave energy through dissipation of such acoustic waves. Therefore, an appropriate treatment of propagation and dissipation of these waves is indispensable in understanding a problem of coronal heating. In this paper, we employ a formulation of a weak-shock theory constructed by SS, originally developed to study acoustic waves generated by convective motions at the photosphere, for propagation and dissipation of the waves produced in the corona. Then, we can explicitly determine the rate of heating by dissipation of the waves on given wave energy flux (or amplitude) and wave period without tuning other free parameters; we do not have to arbitrarily take an exponential type of heating of mechanical energy input,  $F_m \propto \exp(\frac{-(r-R_\odot)}{l_m})$ , for an assumed constant dissipation length,  $l_m$ , which is poorly supported by fundamental physical processes, although this conventional shape of the heating law was adopted, for lack of an alternative in most previous models (Kopp & Orrall 1976; Withbroe 1988; Sandbæk & Leer 1994), to study the global coronal structure.

The paper is organized as follows: In §2, we present our model. We briefly summarize the generation of acoustic waves in the corona (§2.1), and the weak-shock theory formulated by SS (§2.2). Basic equations describing the global coronal structure from  $1R_\odot$  to  $\gtrsim 1\text{AU}$  are shown in §2.3, and we present our method to construct a unique coronal solution on given wave parameters. In §3 we show our model results. First, we discuss variation of coronal wind structures with respect to input parameters from a theoretical point of view (§3.1). Second, we examine several characteristic properties of the resultant corona (§3.2). Finally, we test whether our model is able to reproduce recent observed results for the low-speed wind in the mid- to low-latitude region (§3.3). In §4, we summarize our results and discuss

related topics.

## 2. Model

### 2.1. Generation of Acoustic Waves in the Corona

As a new relevant process of coronal heating in the quiet-Sun region, S99 proposed a model of network-field magnetic reconnection at the chromospheric level. The chromosphere, specially at the minimum-temperature location, is quite a favorable site for reconnection to occur, since the magnetic resistivity is greatest, and the width of the current sheet, which is possibly scaled with the pressure scale height, is smallest there. Such reconnection events form a new closed magnetic flux tube, which is initially located far from the equilibrium state, and hence, will spring upward quickly (consult S99 for a schematic picture). The tube would oscillate about the equilibrium state normal to the solar surface with a period of  $\tau = 2L/v_A$ , where  $v_A$  is Alfvén velocity and  $L$  is the length of the tube. If we use the quoted values in S99 as a typical example of the tube,  $L \sim 1.5 \times 10^9$  cm, a mean magnetic field,  $\sim 100$  G, and a mean density,  $\sim 10^{-12}$  g cm $^{-3}$ , the oscillation periods would be  $\tau \sim 100$  s. It could keep oscillating several tens of times before it is damped (S99). As a result, these perpendicular oscillations would excite longitudinal waves traveling in the vertical direction. Given that the configurations of the magnetic fields are perpendicular above the flux tube, such waves would propagate upwardly as acoustic waves in the rarefied atmosphere. They must contribute to the heating of the surrounding corona directly by the dissipation of the waves.

Using a simple kinetic model, RSW have estimated the energy liberated by the above mechanism as a function of a mean magnetic field strength at the photospheric level. They showed that the mean field of  $\sim 10$  G could generate the required heating rate ( $\gtrsim 10^{5.5}$  erg cm $^{-2}$ s $^{-1}$ ) to explain the conditions in the quiet-Sun region. A sizable fraction of the released energy is supposed to be transported to the energy of the acoustic waves. In our model, we parameterize the input energy flux of the acoustic waves (not the total energy liberated by the reconnection) as  $F_{w,0}$  (erg cm $^{-2}$ s $^{-1}$ ). In this paper, to study the physical processes clearly, we focus on the role of such acoustic waves in the coronal heating and construct the coronal structure on the input  $F_{w,0}$  and wave period  $\tau$ , though some of the released energy would be transformed into other MHD waves depending on complex configurations of magnetic fields (Tarbell, Ryutova, & Covington 1999; Sakai et al. 2000).

We would like to remark that other mechanisms also predict production of longitudinal waves at the coronal height, although we have taken up the chromospheric reconnection

model as a typical process in this paper. Generation of spicules in an open magnetic flux tube have been investigated by various authors (Hollweg, Jackson, & Galloway 1982; Hollweg 1992; Kudoh & Shibata 1999). They found that Alfvén waves excited by random motions at the photosphere (Ulrich 1996) effectively transport their energy to the corona. The nonlinear effect of torsional Alfvén waves produces longitudinal waves along the vertical flux tube in the corona. A sizable fraction of the initial energy of the transverse waves at the photosphere is converted to energy of the longitudinal waves at the coronal height, and these waves could become acoustic waves propagating upwardly. They could heat the surrounding plasma in the very same way as those triggered by the reconnection events above. Thus, acoustic waves are expected to be universally generated by various mechanisms in the corona far above the photosphere, and therefore, it is quite worth studying their role in coronal heating.

## 2.2. Dissipation of Acoustic Waves in Corona

In this section, we describe our method of treating the outward propagation of acoustic waves, after they have been excited in the corona. We first estimate a distance acoustic waves travel before forming shocks on a plane-parallel geometry. Then, we derive an equation dealing with variation of N-wave amplitude on spherical geometry. For simplicity's sake, in the following discussions, we neglect the effects of magnetic field on the propagation of the waves. This simplification is valid when the circumstantial magnetic configuration is perpendicular above the flux tube generating the waves.

### 2.2.1. A Distance Acoustic Waves Travel Before Forming Shocks

Any acoustic wave having a finite amplitude inevitably changes its shape, makes the wave front steepen and eventually forms the shock front (e.g. Landau & Lifshitz 1959). The distance the acoustic waves travel before forming the shocks can be estimated on a given wave length,  $\lambda$ , and initial amplitude,  $\delta v_0$ . Consider the acoustic waves propagating in the upward direction,  $z$ , in isothermal atmosphere with density structure of  $\rho = \rho_0 \exp(-z/H_\rho)$ . Assuming waves having initially sinusoidal velocity profiles,  $\delta v = \delta v_0 \sin(2\pi Z/\lambda)$ , the wave crest overtakes the preceding trough to form a shock front at

$$z - z_0 = 2H_\rho \ln\left(1 + \frac{1}{4(\gamma + 1)} \frac{\lambda}{H_\rho} \frac{c_s}{\delta v_0}\right) \quad (1)$$

(SS), where  $z_0$  is the position at which the waves are created,  $\gamma = 5/3$  is a ratio of specific heat, and  $c_s$  is a sound velocity.

In our calculations, waves of the initial amplitude,  $\delta v_0/c_s = 0.1 \sim 1$  are considered (§3.1), and therefore, the second term in the logarithm in eq.(1) will be bounded by an upper limit:

$$\frac{1}{4(\gamma+1)} \frac{\lambda}{H_\rho} \frac{c_s}{\delta v_0} \lesssim \frac{\lambda}{H_p} = \left(\frac{c_s^2}{\gamma g}\right)^{-1} c_s \tau \simeq 0.25 \left(\frac{\tau}{100\text{s}}\right) \left(\frac{c_s}{2 \times 10^7 \text{cm s}^{-1}}\right)^{-1} \quad (2)$$

where  $g$  is acceleration of gravity, and we have used  $H_\rho \simeq H_p$  which is satisfied in the corona where temperature varies slowly within a scale of  $\lambda (\sim 10^9 \text{cm})$ . Then, eq.(1) can be expanded to a first order as

$$z - z_0 \simeq \frac{\lambda}{2(\gamma+1)} \frac{c_s}{\delta v_0}. \quad (3)$$

The factor  $\frac{1}{2(\gamma+1)} \frac{c_s}{\delta v_0}$  is an order of unity, indicating that after traveling one wave length, the waves begin to dissipate energy.

### 2.2.2. Variation of N-wave amplitude

The initially sinusoidal acoustic waves are expected to be transported as N-waves after the formation of the shocks, provided that they are continuously generated from the lower corona. These N-waves are propagated outwardly in the rarefied atmosphere and dissipate their wave energy to heat the corona. For the purpose of giving a reasonable estimate of heating rate as a function of position, variations of amplitude,  $\delta v_w$ , of the transported N-waves are treated based on the weak-shock theory, following the formulation presented by SS. In the discussions below, propagation of the wave train are considered in a flow tube with a cross-section of  $A$ , to keep the consistencies with a model for the global corona presented in §2.3.  $A$  is a function of  $r$ , a distance measured from the center of the Sun, and modeled in §2.3 with taking into account non-radial expansion of the flow tube. From now on, all the physical quantities are expressed as functions of  $r$  only, unless explicitly declared.

An equation for the variation of wave amplitude normalized by ambient sound velocity,  $\alpha_w \equiv \frac{\delta v_w}{c_s}$ , can be found from SS:

$$\frac{1}{\alpha_w} \frac{d\alpha_w}{dr} = \frac{1}{2} \left( -\frac{1}{p} \frac{dp}{dr} + \frac{1}{E_\lambda} \frac{dE_\lambda}{dr} - \frac{1}{\lambda} \frac{d\lambda}{dr} \right). \quad (4)$$

where  $p$  is gas pressure, and  $E_\lambda = \frac{1}{3} \rho (\delta v_w)^2 \lambda = \frac{1}{3} \gamma p \alpha_w^2 \lambda$  is a wave energy per wave length,  $\lambda$ . The variation of the wave energy can be estimated from entropy generation by the weak shock (SS; §56 in Mihalas & Mihalas 1984) as

$$\nabla \cdot E_\lambda = \frac{dE_\lambda}{dr} + \frac{E_\lambda}{A} \frac{dA}{dr} = -E_\lambda \frac{2(\gamma+1)\alpha_w}{\lambda} \simeq -E_\lambda \frac{2(\gamma+1)\alpha_w}{c_s \tau}, \quad (5)$$

where we have used a relation of  $\lambda = c_s(1 + \frac{\gamma+1}{2}\alpha_w)\tau \simeq c_s\tau$  by assuming  $\alpha_w < 1$ . In general, the period of waves traveling in different media remains as a constant, implying  $\frac{1}{\lambda}\frac{d\lambda}{dr} = \frac{1}{c_s}\frac{dc_s}{dr}$ . Hence, eq.(4) is reduced to

$$\frac{d\alpha_w}{dr} = \frac{\alpha_w}{2}\left(-\frac{1}{p}\frac{dp}{dr} - \frac{2(\gamma+1)\alpha_w}{c_s\tau} - \frac{1}{A}\frac{dA}{dr} - \frac{1}{c_s}\frac{dc_s}{dr}\right). \quad (6)$$

This equation determines the variation of the wave amplitude in the solar corona according to the physical properties of the background coronal plasma. The first term in the r.h.s. is positive in the density decreasing atmosphere, and the second term of the entropy generation (heating) is negative. In the  $(1-2)R_\odot$  region, where the dissipation is important to heat the corona, these two terms always dominate the other terms, the third term arising from the geometrical expansion and the fourth due to temperature variation. Using  $\alpha_w$  determined above as well as background physical quantities,  $\rho$  and  $c_s$ , wave energy flux,  $F_w$  (erg cm<sup>-2</sup>s<sup>-1</sup>), is derived as

$$F_w = \frac{1}{3}\rho c_s^3(\alpha_w)^2\left(1 + \frac{\gamma+1}{2}\alpha_w\right), \quad (7)$$

if recalling that the wave crest moves at a speed of  $c_s(1 + \frac{\gamma+1}{2}\alpha_w)$ .

Since the model described above is simple, we instead have several limitations that should be taken into account with great care. The first obvious limitation is that the wave amplitude should satisfy the assumption of weak-shock,  $\alpha_w < 1$ . Second, it does not take into account the effects of gravity. Third, it is constructed in a static medium, therefore we cannot apply it to cases of moving media, such as N-waves in the solar wind where the flow velocity,  $v$ , exceeds the ambient  $c_s$ . Of the three limitations, the third one is most easily overcome, because in all the cases we calculate in this paper, at least 99% of the initial wave energy dissipates within  $r < 1.3R_\odot$ , the region where  $v \ll c_s$  is fulfilled (figs.1 & 2). The second limitation also seems to have little effect if the wave period is small enough, since SS found that the weak-shock theory gives reasonable estimates for waves of  $\tau < \frac{1}{2}\frac{2\pi}{\omega_{ac}}$ , where  $\omega_{ac} = \frac{\gamma g}{2c_s}$  is the acoustic cut-off frequency in a gravitationally stratified atmosphere, after comparing results of the weak-shock theory with those of fully non-linear calculations. As  $\omega_{ac} \simeq \frac{1}{800(\text{s})}\left(\frac{c_s}{2 \times 10^7 \text{cm s}^{-1}}\right)^{-1}$  in the corona, the weak-shock theory seems to be applicable to waves of  $\tau < 2000\text{s}$ . To check whether the first limitation is overcome, we need to calculate a  $\alpha_w$  variation in the solar corona at first hand. Our results show that any waves we calculate give  $\alpha_w < 0.5$  in the entire corona (§3.1). Thus, the weak-shock theory appears to be applicable to our model and to give a reasonable estimate of the heating rate as a function of  $r$ .

### 2.3. Basic Equations

We here present basic equations to describe one-component coronal wind structure in a flow tube with a cross-section of  $A$  under a steady state condition. Then, an equation of continuity becomes

$$\rho v A = \text{const.} \quad (8)$$

An equation of momentum conservation is

$$v \frac{dv}{dr} = -\frac{GM_\odot}{r^2} - \frac{1}{\rho} \frac{dp}{dr} - \frac{1}{\rho c_s (1 + \frac{\gamma+1}{2} \alpha_w)} \nabla \cdot F_w. \quad (9)$$

Pressure,  $p$ , is related to  $\rho$  and temperature,  $T$ , by an equation of state for ideal gas:

$$p = \rho \frac{k_B}{m_H \mu} T, \quad (10)$$

where  $m_H$  is hydrogen mass,  $k_B$  is Boltzmann constant, and  $\mu$  is mean atomic weight of particles in unit of  $m_H$ . The third term in eq.(9) represents wave momentum deposition, neglecting the effects of reflection and refraction (Rosner & Vaiana 1977). Total energy equation is obtained as

$$\nabla \cdot [\rho v (\frac{1}{2} v^2 + \frac{\gamma}{\gamma-1} \frac{k_B}{m_H \mu} T - \frac{GM_\odot}{r}) + F_w + F_c] + q_R = 0, \quad (11)$$

where we adopt the classical form of conductive flux for ionized gas,

$$F_c = -\kappa \frac{dT}{dr} = -\kappa_0 T^{\frac{5}{2}} \frac{dT}{dr}, \quad (12)$$

with  $\kappa_0 = 1.0 \times 10^{-6}$  in c.g.s unit (Allen 1973), and the radiative cooling term,  $q_R$  (erg  $\text{cm}^{-3} \text{s}^{-1}$ ), is derived from tabulated radiative loss function,  $\Lambda$  (erg  $\text{cm}^3 \text{s}^{-1}$ ), (Landini & Monsignori-Fossi 1990) for the optically thin plasma as  $q_R = n_e n_p \Lambda$ , where  $n_e$  &  $n_p$  are electron and  $\text{H}^+$  density respectively. They are calculated by solving ionization of H and He (we ignore heavy elements) under LTE condition. The term,  $\nabla \cdot F_w (\leq 0)$ , in eq.(11) indicates the heating by the dissipation of the waves, which is explicitly written as

$$\nabla \cdot F_w = \begin{cases} 0 & r \leq r_d \\ \rho v [\frac{1}{3} \alpha_w^2 (1 + \frac{\gamma+1}{2} \alpha_w) \frac{d}{dr} (\frac{c_s^3}{v}) + (\frac{2}{3} \alpha_w + \frac{\gamma+1}{2} \alpha_w^2) (\frac{c_s^3}{v}) \frac{d\alpha_w}{dr}] & r > r_d \end{cases}, \quad (13)$$

where  $r_d$  is the position where the waves start to dissipate by shaping N-waves, and the height  $h_d \equiv r_d - R_\odot$  from the photosphere corresponds to the sum of the height of the magnetic flux tube ( $\sim 10^9 \text{cm}$ ; the generation point of the waves) and the distance the acoustic waves travel before forming the shock fronts ( $\sim \lambda \sim 10^9 \text{cm}$ ; eq.(3)). We adopt  $h_d = 2 \times 10^9 \text{cm}$  as a standard value.



To take into account non-radial expansion of the flow tube due to configurations of magnetic field, cross-sectional area,  $A$ , is modeled as

$$A = r^2 \frac{f_{\max} e^{(r-r_1)/\sigma} + f_1}{e^{(r-r_1)/\sigma} + 1} \quad (14)$$

where

$$f_1 = 1 - (f_{\max} - 1)e^{(1-r_1)/\sigma}$$

(Kopp & Orrall 1976; Withbroe 1988). The cross section expands from unity to  $f_{\max}$  most drastically between  $r = r_1 - \sigma$  and  $r_1 + \sigma$ . Of three input parameters,  $f_{\max}$  is the most important in determining solar wind structure. In this paper, we consider cases for  $f_{\max} = 5$  and  $f_{\max} = 1$  (pure radial expansion). As for the rests of the two parameters, we employ  $r_1 = 1.25R_{\odot}$  and  $\sigma = 0.1R_{\odot}$ , the same values adopted in a model for 'quiet corona' in Withbroe (1988).

## 2.4. Boundary Conditions and Computational Method

Now we would like to explain the practical aspects of our method of constructing wind structure with respect to various input properties of the waves. In order to solve both heating of corona (energy transfer) and formation of solar wind (momentum transfer) consistently, our calculation is performed in a broad region from an inner boundary of the upper chromosphere where temperature,  $T_{\text{ch}} = 10^4\text{K}$ , at  $r_{\text{ch}} = R_{\odot} + h_{\text{ch}}$ , which is located at  $h_{\text{ch}} = 2 \times 10^8\text{cm}$  (2000 km) above the photosphere (Allen 1973) to an arbitrary outer boundary at  $r_{\text{out}} = 300R_{\odot}$ .

We set four boundary conditions to construct a unique solution for a given input wave energy flux  $F_{w,0}$  as follows:

$$F_w(r_{\text{ch}}) = F_w(r_{\text{d}}) = F_{w,0}, \quad (15)$$

$$T(r_{\text{ch}}) = T_{\text{ch}}, \quad (16)$$

$$|F_c(r_{\text{ch}})| (\simeq 0) \ll |F_{c,\max}|, \quad (17)$$

$$\nabla \cdot F_c(r_{\text{out}}) = 0, \quad (18)$$

where  $F_{c,\max}$  in eq.(17) is a maximum value of downward conductive flux in the inner corona. The first condition denotes that wave energy flux must agree with a given value when the waves start to dissipate. The second condition is also straightforward: the temperature has to coincide with the fixed value at the inner boundary. The third condition is the requirement that the downward thermal conductive flux should become sufficiently small at the upper chromosphere ( $T = 10^4\text{K}$ ), diminishing from its enormous value at the coronal

base ( $T \sim 10^6\text{K}$ ). Practically, we continue calculations iteratively until  $F_c(r_{\text{ch}})/F_{c,\text{max}} < 1\%$  is satisfied. The fourth condition corresponds to an ordinary requirement that no heat is conducted inward from infinity (Sandbæk & Leer 1994). Note that thanks to the third condition, coronal base density, which is poorly determined from the observations, does not have to be used as a boundary condition. As a result, the number of free parameters to be set in advance is reduced (Hammer 1982a,b; Withbroe 1988). The density at the coronal base or the transition region (TR) is calculated as an output; larger input  $F_{w,0}$  increases downward  $F_c$  in the lower corona, demanding larger density in the coronal base and TR to enhance radiative cooling to balance with the increased conductive heating.

For numerical integration of the momentum equation (eq.(9)) and the energy equation (eq.(11)), we respectively use  $v$  and an isothermal sound velocity,  $a$ , defined as

$$a^2 = \frac{c_s^2}{\gamma} = \frac{p}{\rho} = \frac{k_B}{m_H \mu} T. \quad (19)$$

To carry out the integration, the equations shown in the previous section need to be transformed into useful forms. First, an expression for velocity gradient can be written from eqs.(8),(9), & (10):

$$\frac{dv}{dr} = \frac{-\frac{GM_\odot}{r^2} + \frac{a^2}{A} \frac{dA}{dr} - \frac{da^2}{dr}}{v - \frac{a^2}{v}} \quad (20)$$

Second, an expression for gradient of  $a^2$  is derived from an integrated form of eq.(11):

$$\frac{da^2}{dr} = \frac{\rho v}{\kappa_0 a^5} \left( \frac{k_B}{m_H \mu} \right)^{\frac{7}{2}} \left( \frac{v^2}{2} + \frac{\gamma}{\gamma - 1} a^2 - \frac{GM_\odot}{r} + \frac{F_w}{\rho v} + \int_{r_0}^r dr \frac{q_R}{\rho v} - E_{\text{tot}} \right), \quad (21)$$

where,  $r_0$  is a certain reference point of integration that will be set later.  $E_{\text{tot}}$  is mathematically an integral constant, which must be conserved in the entire region of the calculation.

Only transonic solutions are allowed for the flow speed,  $v$ . The integration of three differential equations (20),(21), and (6) is carried out simultaneously from the sonic point,  $r = r_s$  to both outward and inward directions by the fourth-order Runge-Kutta method, also deriving density from eq.(8) at each integration. We have used variable sizes for the grid of the integration, setting the smaller mesh size in the region where physical values change rapidly. For instance, in the TR, we set a mesh as small as  $10^3$  cm (0.01 km) for one grid. To start the integration, we have to set nine variables,  $v_s$ ,  $(\frac{dv}{dr})_s$ ,  $a_s^2$ ,  $(\frac{da^2}{dr})_s$ ,  $\alpha_{w,s}$ ,  $(\frac{d\alpha_w}{dr})_s$ ,  $\rho_s$ ,  $E_{\text{tot}}$  and  $r_s$  (subscript 's' denotes the sonic point). We can determine  $v_s$ ,  $(\frac{dv}{dr})_s$  and  $r_s$  for given  $a_s^2$  and  $(\frac{da^2}{dr})_s$  by a condition that both the numerator and the denominator of eq.(20) are zero at  $r_s$  (Parker 1958).  $(\frac{d\alpha_w}{dr})_s$  is also derived from eq.(6) on a given  $\alpha_{w,s}$ . Setting the reference point,  $r_0 = r_s$ , for the integration of radiative cooling function, we obtain  $E_{\text{tot}}$  as

$$E_{\text{tot}} = \left[ \frac{1}{2} v^2 + \frac{\gamma}{\gamma - 1} a^2 - \frac{GM_\odot}{r} + \frac{F_w}{\rho v} - \left( \frac{m_H \mu}{k_B} \right)^{\frac{7}{2}} \frac{1}{\rho v} \kappa_0 a^5 \left( \frac{da^2}{dr} \right) \right]_s, \quad (22)$$

where all the variables are evaluated at the sonic point. Now we have four variables,  $a_s^2$ ,  $(\frac{da^2}{dr})_s$ ,  $\alpha_{w,s}$ , and  $\rho_s$ , remaining to be regulated by the four boundary conditions of eqs.(15)–(18). Concrete procedures for finding a unique solution on a given  $F_{w,0}$  are described below.

1. One makes an initial guess for  $[a_s^2, (\frac{da^2}{dr})_s, \alpha_{w,s}, \rho_s]$ .
2. The integration is performed in the outward direction from  $r_s$ . Leaving  $a_s^2, \alpha_{w,s}, \&\rho_s$  unchanged,  $(\frac{da^2}{dr})_s$  are determined by carrying out the integration iteratively to satisfy the outer boundary condition of eq.(18).
3. The integration is performed iteratively in the inward direction, improving  $a_s^2, \alpha_{w,s}$ , and  $\rho_s$  for the fixed  $(\frac{da^2}{dr})_s$  until they satisfy the three inner boundary conditions, eqs.(15)–(17). Physically, the condition of the wave flux (eq.(15)) regulates  $\alpha_{w,s}$ , that of temperature (eq.(16)) regulates  $a_s^2$ , and that of the conductive flux (eq.(17)) regulates  $\rho_s$ . These relations guide improvement of the respective initial guesses, though they are not independently approved. Unless the above inner boundary conditions are satisfied simultaneously, one returns to procedure 2, preparing a new set of  $[a_s^2, (\frac{da^2}{dr})_s, \alpha_{w,s}, \rho_s]$ .
4. One can finally find a unique solution by iterating procedures 2 and 3.

### 3. Results

#### 3.1. Theoretical Interpretation of Resultant Coronal Structures

Figure 1 demonstrates our result of coronal wind structures employing the same input  $F_{w,0} = 7.8 \times 10^5 \text{ erg cm}^{-2} \text{ s}^{-1}$ , but different sets of wave periods and non-radial expansion factors,  $(\tau(s), f_{\text{max}}) = (300, 5), (60, 5), (300, 1)$ . Figure 2 compares the wind structures adopting three different  $F_{w,0} = (3.2, 5.9, 10) \times 10^5 \text{ erg cm}^{-2} \text{ s}^{-1}$  for identical inputs of  $\tau = 120\text{s}$  and  $f_{\text{max}} = 5$ . Distribution of temperature, flow velocity, and electron density from the inner boundary to 1AU ( $= 215R_{\odot}$ ) are displayed from top to bottom on the left side of the both figures. On the right side, we present variation of wave amplitude,  $\alpha_w$ , a dissipation length,  $l_w$ , of N-waves, which is defined as  $l_w = \frac{F_w}{\nabla \cdot F_w}$ , and heating per unit mass,  $|\frac{1}{\rho v} \nabla \cdot F_w|$ , respectively. In tab.1, we tabulated several resultant properties of the corona and solar wind as well as the input parameters.

To begin with, we would like to emphasize that corona heats up to  $> 10^6\text{K}$  in every case, because acoustic waves generated in the corona are able to heat the surrounding gas directly, unlike acoustic waves produced at the photosphere. However, N-waves are rapidly damped, so that the heating occurs only in inner region as seen in the lower right panels of

Input	Output				
$(F_{w,0}, \tau, f_{\max})$	$p_{\text{tr}}$	$T_{\max}$	$r_{T_{\max}}$	$(n_p v)_{1\text{AU}}$	$(v)_{1\text{AU}}$
(7.8, 60, 5)	0.28	1.43	1.04	$3.8 \times 10^6$	222
(7.8, 300, 5)	0.24	1.50	1.08	$7.5 \times 10^7$	251
(7.8, 300, 1)	0.29	1.71	1.12	$3.8 \times 10^8$	222
(3.2, 120, 5)	0.13	1.16	1.05	$2.5 \times 10^6$	230
(5.9, 120, 5)	0.21	1.35	1.05	$1.3 \times 10^7$	240
(10, 120, 5)	0.32	1.52	1.05	$1.3 \times 10^7$	230

Table 1: Input parameters and output wind properties of each model;  $F_{w,0}$  is in  $10^5 \text{erg cm}^{-2} \text{s}^{-1}$  and  $\tau$  in second.  $p_{\text{tr}}$  is pressure in  $\text{dyn cm}^{-2}$  at the TR where  $T = 10^5 \text{K}$ ,  $T_{\max}$  is peak coronal temperature in  $10^6 \text{K}$ ,  $r_{T_{\max}}$  is location of  $T_{\max}$  in  $R_{\odot}$ ,  $(n_p v)_{1\text{AU}}$  is proton flux in  $\text{cm}^{-2} \text{s}^{-1}$  at 1AU, and  $(v)_{1\text{AU}}$  is the flow velocity in  $\text{km/s}$  at 1AU.

figs.1 and 2. Then, location of maximum temperature,  $T_{\max}$ , is quite close to the surface. In an outside region of  $\gtrsim 1.5R_{\odot}$ , heat is input only by outward thermal conduction, and the flow is accelerated mostly by thermal pressure. As a result, speed of the solar wind at 1AU is  $\lesssim 300 \text{km/s}$ , which is slightly slower than the actual low-speed wind ( $300 \sim 450 \text{km/s}$ ).

The top right panel of fig.2 interestingly illustrates that distributions of  $\alpha_w$  are almost identical in spite of very different inputs of  $F_{w,0}$ . Particularly, initial N-wave amplitudes,  $\alpha_w(r_d)$ , at  $r_d$ , are within a range between 0.48 and 0.49. This is because  $F_{w,0}$  ( $\sim p\alpha_{w,0}^2 c_s$ ; eq.(7)) mostly owes its variation to change of ambient pressure (see §3.2.1). Moreover, an upper right panel of fig.1 also indicates that initial  $\alpha_w$  ( $\simeq 0.5$ ) is almost independent of  $\tau$  and  $f_{\max}$ . We have found that  $0.45 < \alpha_w(r_d) < 0.52$  within our parameter regions of  $F_{w,0} = (1 - 20) \times 10^5 \text{erg cm}^{-2} \text{s}^{-1}$ ,  $\tau = 60 - 300 \text{s}$ , and  $f_{\max} = 1 - 5$ . This proves that  $\alpha_w < 1$  is fulfilled in the entire region, which justifies the assumption of weak shock. Middle right panels of figs.1 and 2 show that the dissipation length is a drastically varying function on  $r$ . This implies that the assumption of a constant dissipation length usually taken in previous models for the global corona (Withbroe 1988; Sandbæk & Leer 1994) is very poor for our N-wave process.

In the following discussions, we examine dependences of the wind structures on the respective input parameters. First, we argue dependences on wave periods. As illustrated in fig.1, N-waves with smaller  $\tau$  dissipate more quickly and the heating occurs in thinner region close to the surface. This simply leads to deposition of wave energy in denser region. Since radiative loss,  $q_R$  ( $\text{erg cm}^{-3} \text{s}^{-1}$ ), is in proportion to  $\rho^2$  for optically thin plasma, a greater fraction of energy supplied in denser region goes into radiative escape. Consequently, a smaller amount of energy remains to heat the corona and accelerate the flow. The case adopting

smaller  $\tau$ (=60s) gives lower temperature in the corona, and therefore, a smaller pressure scale height and a more rapid decrease of density, as shown in fig.1. Lower temperature also takes the sonic point more distant from the solar surface, and then, mass flux of the solar wind becomes much smaller than that expected from the  $\tau = 300$ s case (tab.1).

Second, we study effects on areal expansion of the flow tube. Comparing results adopting the same  $F_{w,0} = 7.8 \times 10^5 \text{erg cm}^{-2}\text{s}^{-1}$  and  $\tau = 300$ s but different  $f_{\text{max}} = 1$  and 5 in fig.1, one can notice significant change of density structure. The model considering the non-radial expansion gives more drastic decrease of density as a function of  $r$  in spite of similar initial density at the inner boundary. Temperature in the inner corona is also lower in that model, since more fraction of the input energy is lost adiabatically due to geometrical expansion of the flow tube. On the other hand, decrease of temperature is slower and temperature in the outer region ( $\gtrsim 8R_{\odot}$ ) is higher. This is because the lower density reduces both radiative cooling and adiabatic loss. The higher temperature also leads to larger acceleration of the flow there, giving larger speed of the solar wind in the outer corona.

Third, we investigate dependencies on input wave energy flux. Models employing larger input  $F_{w,0}$  give larger density in the inner corona (fig.2), because radiative cooling should be raised to offset the increased heating. More accurately, larger input  $F_{w,0}$  results in larger downward conductive flux from the corona to the chromosphere, which needs larger radiative cooling to balance with enhanced conductive heating. Larger  $F_{w,0}$  also leads to higher temperature in the inner corona. However, more rapid decrease of temperature occurs because of enhanced radiative escape. A model employing  $F_{w,0} = 10 \times 10^5 \text{erg cm}^{-2}\text{s}^{-1}$  yields lower temperature in a region of  $r \gtrsim 1.5R_{\odot}$  than that adopting  $F_{w,0} = 5.9 \times 10^5 \text{erg cm}^{-2}\text{s}^{-1}$ . Therefore, a larger input of  $F_{w,0}$  does not simply anticipate larger acceleration of the flow, and relations of  $F_{w,0} - (n_p v)_{1\text{AU}}$  and  $F_{w,0} - (v)_{1\text{AU}}$  does not show simple positive correlations (tab.1, see also §3.2.2)

## 3.2. Some Characteristic Properties of Resultant Corona

### 3.2.1. Peak Temperature and Pressure at the TR

We would like to inspect relations of peak coronal temperature,  $T_{\text{max}}$ , and pressure,  $p_{\text{tr}}$ , at the TR with respect to the input model parameters. In fig.3, we present  $T_{\text{max}}$  as a function of input  $F_{w,0}$  for different  $\tau$  and  $f_{\text{max}}$ . The figure shows that  $T_{\text{max}} > 10^6 \text{K}$  is accomplished for  $F_{w,0} \geq 2 \times 10^5 \text{erg cm}^{-2}\text{s}^{-1}$ , even if one chooses waves with a short period ( $\tau = 60$ s) and a large expansion factor ( $f_{\text{max}} = 5$ ).  $T_{\text{max}}$  is a monotonically increasing function of  $F_{w,0}$  on

each set of  $(\tau, f_{\max})$ , and the relations can be fitted by power-law as

$$T_{\max} \propto (F_{w,0})^k, \quad \text{where} \quad k = 0.23 - 0.26. \quad (23)$$

Figure 4 displays relations between  $F_{w,0}$  and  $p_{\text{tr}}$ .  $p_{\text{tr}}$  is evaluated at  $T = 10^5\text{K}$ , whereas  $p_{\text{tr}}$  is almost a constant through the TR from the upper chromosphere ( $T \simeq 10^4\text{K}$ ; inner boundary) to the coronal base ( $T \simeq 5 \times 10^5\text{K}$ ) because of its geometrically thin configuration. The figure indicates that  $p_{\text{tr}}$  weakly depends on  $\tau$  and  $f_{\max}$ , and has a positive correlation with  $F_{w,0}$ :

$$p_{\text{tr}} \propto (F_{w,0})^l, \quad \text{where} \quad l = 0.75 - 0.79 \quad (24)$$

A rise of  $F_{w,0}$  leads directly to an increase in downward conductive flux, which demands higher density (or pressure) in the lower corona and the TR to raise radiative cooling to balance with the enhanced conductive heating. Alternatively, it could be interpreted that injection of larger energy in the corona can heat more deeply to the higher density chromosphere by the downward thermal conduction.

A combination of the above two relations of eqs.(23) and (24) roughly give

$$T_{\max} \propto (p_{\text{tr}})^{1/3},$$

on given  $\tau$  and  $f_{\max}$ , which reminds us of the famous RTV scaling law (Rosner, Tucker, & Vaiana 1978),  $T_{\max} \simeq 1400(p_1 L_h)^{1/3}$ , for closed magnetic loops, where  $p_1(\text{dyn cm}^{-2})$  is loop pressure and  $L_h(\text{cm})$  is loop height. Taking  $r_{T_{\max}}$  instead of  $L_h$  for our model, we can actually derive a relation between  $T_{\max}$  and  $(p_{\text{tr}} r_{T_{\max}})$  from our results as

$$T_{\max} \simeq 3000(p_{\text{tr}} r_{T_{\max}})^{0.30},$$

showing a form analogous to that of the original RTV law. This is because we consider the same energy balance among thermal conduction, radiative cooling, and heating with the same boundary condition that the conductive flux should become almost zero at the base (eq.(17)), although the configurations are quite different (closed loop for the RTV law and open flow tube for ours). The slight discrepancies of the prefactor and power-law index are caused by the fact that the RTV law was derived on the assumption of spatially uniform heating along the loop, while our heating function is determined by eq.(13), which is not uniform at all.

### 3.2.2. Mass Flux and Coronal Energy Loss

In fig.5 we show anticipated proton flux,  $(n_p v)_{1\text{AU}}$ , at 1AU as a function of  $F_{w,0}$  for different  $\tau$  and  $f_{\max}$ , with observational constraints,  $(n_p v)_{1\text{AU}} = (3.8 \pm 1.5) \times 10^8 \text{cm}^{-2} \text{s}^{-1}$

(Shaded), compiled by Withbroe (1988) as the empirical value for 'quiet corona' which is supposed to corresponds to the mid- to low-latitude region generating the low-speed wind. Larger  $\tau$  waves give a greater  $(n_p v)_{1\text{AU}}$  owing to the effective transport of dissipated energy to solar wind flow by avoiding radiative escape. Introduction of the non-radial expansion of the flow tube reduces  $(n_p v)_{1\text{AU}}$ , because input energy per unit flow tube normalized at 1AU decreases on increasing  $f_{\text{max}}$ , even though one inputs identical wave energy flux at the inner corona. Therefore, the larger areal expansion straightforwardly reduces mass flux of the solar wind. As to dependences on  $F_{w,0}$ ,  $(n_p v)_{1\text{AU}}$  has an upper limit for given  $\tau$  and  $f_{\text{max}}$ . (Even models of  $\tau = 300\text{s}$  and  $f_{\text{max}} = 1$  are supposed to have the upper limit in a  $F_{w,0} > 2 \times 10^6 \text{erg cm}^{-2} \text{s}^{-1}$  area.) Figure 5 shows that only one case employing  $(\tau, f_{\text{max}}) = (300, 1)$  can reproduce observed proton flux of the slow wind. Unfortunately more realistic cases considering the non-radial expansion of  $f_{\text{max}} = 5$  cannot explain the observations, which implies that other mechanisms of heating (and acceleration) necessarily work cooperatively.

We would like to study in detail why  $(n_p v)_{1\text{AU}}$  has an upper limit on fixed  $\tau$  and  $f_{\text{max}}$ . Figure 6 displays the ratios of the main three types of energy loss: downward thermal conduction from the coronal base, radiative escape in the corona, and total amount of energy converted to the flow (mass loss) at  $r_{\text{out}}$ , respectively normalized by  $F_{w,0}$  for the cases adopting  $\tau = 120\text{s}$  and  $f_{\text{max}} = 5$ . The values for downward thermal conduction in fig.6 are taken from maximum conductive flux  $F_{c,\text{max}}$  in lower corona (see fig.7) and the values for the radiative escape are derived by the integration of the radiative cooling function from points with  $F_{c,\text{max}}$  to  $r_{\text{out}}$ . The region not labeled between 'radiative escape' and 'flow' denotes energy carried out of  $r_{\text{out}}$  by thermal conduction. According to fig.6, the main source of coronal energy loss is downward thermal conduction within our range of  $F_{w,0}$  (strictly speaking, most of the conducted energy finally radiates away), whereas radiative escape comes to play a significant role for larger  $F_{w,0}$  since density in the corona becomes higher, being subject to eq.(24). Although a ratio of energy transferred to the flow is as small as  $\lesssim 3\%$  throughout the range, it has a bimodal tendency. In  $F_{w,0} < 6 \times 10^5 \text{erg cm}^{-2} \text{s}^{-1}$  it increases, which implies that the larger  $F_{w,0}$  is, the more effectively the energy is transferred to the flow. However, in  $F_{w,0} > 6 \times 10^5 \text{erg cm}^{-2} \text{s}^{-1}$ , it decreases because of the abrupt dominance of radiative cooling. As a result, the predicted  $(n_p v)_{1\text{AU}}$  increases rapidly on increasing  $F_{w,0}$  at first and eventually decreases as seen in fig.5.

To examine these differences in terms of energy transfer, we show variations of energy flux of four components,

$$\text{wave} : f_w = \frac{A(r)}{A(r_{\text{ch}})} F_w, \quad (25)$$

$$\text{conduction : } f_c = \frac{A(r)}{A(r_{\text{ch}})} F_c, \quad (26)$$

$$\text{flow : } f_f = \rho v \frac{A(r)}{A(r_{\text{ch}})} \left[ \left( \frac{1}{2} v^2 + \frac{\gamma}{\gamma - 1} a^2 - \frac{GM_{\odot}}{r} \right) - \left( \frac{1}{2} v^2 + \frac{\gamma}{\gamma - 1} a^2 - \frac{GM_{\odot}}{r} \right)_{r_{\text{ch}}} \right], \quad (27)$$

$$\text{radiation : } f_R = \rho v \frac{A(r)}{A(r_{\text{ch}})} \int_{r_{\text{ch}}}^r dr \frac{q_R}{\rho v}, \quad (28)$$

per flow tube with a cross section of  $A = 1 \text{cm}^2$  at the inner boundary. The 'flow' term of eq.(27) contains three ingredients, kinetic energy of the solar wind, enthalpy, and gravitational energy. Note that, except the wave energy flux, the zero point of the energy is taken here at the inner boundary, to clarify what fraction of the input energy flux is transferred to the other components. In a left panel of fig.7, the status of energy transfer in the inner corona is displayed in a linear scale for both X and Y-axis, and in a right panel, that in the broader region is shown in log scale. The ratio of the downward thermal conduction,  $f_c/F_{w,0}$ , is smaller for larger  $F_{w,0}$ , though the absolute value of  $F_c$  is increasing along with  $F_{w,0}$ . At the TR, most of the heat flux by the downward conduction finally escapes as radiation, except for a tiny fraction transferred to the enthalpy to be used to heat the TR. This leads to a smaller ratio of the radiative loss,  $f_R/F_{w,0}$ , for larger  $F_{w,0}$  in the inner region of  $< 1.2R_{\odot}$ . However, the contribution from the radiation continues in a much more distant region in the model employing largest  $F_{w,0}$ , and  $f_R/F_{w,0}$  finally outdoes the other two cases. Consequently, the ratio of energy transferred to the solar wind becomes smaller than the model adopting smaller  $F_{w,0} (= 5.9 \times 10^5 \text{erg cm}^{-2} \text{s}^{-1})$  as seen in the right panel. It can be concluded that if  $F_{w,0}$  is larger than a certain threshold, an increase of the input  $F_{w,0}$  does not lead to effective heating of the corona to accelerate the solar wind but results in deposition of the wave energy in the high density region to be wasted as radiative escape.

### 3.2.3. Wave Amplitude in the Inner Corona

Ultraviolet and X-ray emission lines of the corona show non-thermal broadenings (Hasler et al. 1990; Erdélyi et al. 1998), which are inferred to originate from wave motions. We investigate whether the obtained wave amplitudes are consistent with these observations. In tab.2, we show our results of the wave rms velocities in the inner corona, which are calculated as

$$\langle \delta_w \rangle = \frac{1}{\sqrt{3}} \delta_w$$

for the N-shaped wave. As the waves propagate upwardly from a location of  $T = 5 \times 10^5 \text{K}$  to that of  $T = 10^6 \text{K}$ , the wave amplitude increases according as the ambient density decreases. Our models give the very similar results for different  $F_{w,0}$  (also  $\tau$  and  $f_{\text{max}}$ ), since change of



Input	$\langle \delta_w \rangle$	
	$T = 5 \times 10^5 \text{K}$	$T = 10^6 \text{K}$
$(F_{w,0}, \tau, f_{\max})$		
(7.8, 60, 5)	32	42
(7.8, 300, 5)	34	44
(7.8, 300, 1)	32	41
(3.2, 120, 5)	31	41
(5.9, 120, 5)	32	42
(10, 120, 5)	34	44

Table 2:  $\langle \delta_w \rangle$ (km/s) in the inner corona

$F_{w,0}$  ( $\sim \rho \langle \delta_w \rangle^2 c_s$ ) mostly reflects variation of the density (fig.2 and §3.1). The tabulated results are marginally consistent with non-thermal velocities of  $20 \sim 40 \text{km/s}$  obtained from observations of inner coronal lines in the solar disks and limbs (Erdélyi et al. 1998), if we assume the observed non-thermal components totally consist of the waves of the acoustic mode. However, this assumption may be too extreme, because other modes of the waves actually exist in the real solar corona.

### 3.3. Comparison of Coronal Wind Structure with Observed Low-Speed Wind

In this section, we study a feasibility of the process of acoustic waves in the coronal heating by comparing our results with recent observations. Aiming at coronal heating and wind acceleration in a region where the low-speed wind is formed, we take observational data of the coronal streamer in the mid- to low-latitude region.

#### 3.3.1. Density Distribution

In fig.8, we display our results of electron density with observation of the streamer (Parenti et al. 2000; Hayes, Vourlidas, & Howard 2001). Our models adopt an identical  $F_{w,0} = 7.8 \times 10^5 \text{erg cm}^{-2} \text{s}^{-1}$  and three sets of  $(\tau(s), f_{\max}) = (300, 5), (60, 5), (300, 1)$  (same as fig.1). As for the observation, we show results derived from a line ratio of Si IX by CDS/SOHO for a region of  $1.02 - 1.19 R_\odot$ , a ratio of radiative and collisional intensities of O VI line by UVCS/SOHO for a region of  $1.58 - 1.6 R_\odot$  (Parenti et al. 2000), and total brightness obtained from LASCO/SOHO for a region  $1.5 R_\odot \lesssim r \lesssim 6 R_\odot$  (Hayes, Vourlidas, & Howard 2001). With respect to the CDS and UVCS data, both results for equatorial and mid-latitude streamer regions are displayed.

Our results, adopting the same  $F_{w,0}$ , show almost identical density in very inner part, being independent of  $\tau$  and  $f_{\max}$  (§3.2.1 and fig.4). The figure exhibits that the adopted value,  $F_{w,0} = 7.8 \times 10^5 \text{erg cm}^{-2}\text{s}^{-1}$ , reproduces the CDS observation of the mid-latitude streamer well. To fit to the data of the equatorial streamer, slightly smaller input of  $F_{w,0}$  is favored. In our model,  $\tau$  and  $f_{\max}$  control slope of density distribution.  $\tau$  influences temperature in an intermediate region of  $2R_{\odot} \lesssim r \lesssim 10R_{\odot}$  (fig.1), hence, regulates the density scale height (or decreasing slope of density) in that region. The data based on LASCO/SOHO indicates that models considering larger  $\tau$ (=300s) are more likely.  $f_{\max}$  determines density decrease in a region of  $1 \sim 2R_{\odot}$ . The data of CDS ( $\lesssim 1.2R_{\odot}$ ) and UVCS ( $\sim 1.6R_{\odot}$ ) exhibits the drastic decrease of density, which indicates that non-radial expansion is desired. Adjustment of the other parameters of the flow tube geometry ( $r_1$  and  $\sigma$ ; eq.(14)) would give the still better fit. Although we do not further search the best parameter set to fit to the observation, the figure indicates that our model could reproduce the observed density profile by the choice of the appropriate parameters ( $F_{w,0} \simeq (5 - 8) \times 10^5 \text{erg cm}^{-2}\text{s}^{-1}$ ,  $\tau \approx 300\text{s}$ , and  $f_{\max} \approx 5$ ).

### 3.3.2. Temperature Distribution

Figure 9 compares our results of temperature distribution with observation in the streamer region. Our models employ the same parameter sets as in fig.8, and the data were electron temperature obtained from observations of a line ratio of Fe XIII/Fe X by the CDS and UVCS/SOHO (Parenti et al. 2000). Although the observed data are electron temperature, they are supposed to represent the plasma temperature because electron-ion equilibrium is attained in dense streamer region of  $r \lesssim 2R_{\odot}$  (Raymond et al. 1998). Therefore, it is reasonable to compare them to the results of our model considering one-fluid coronal plasma. A case employing  $(F_{w,0}, \tau, f_{\max}) = (7.8 \times 10^5, 300, 5)$  gives reasonable peak temperature of  $\simeq 1.5 \times 10^6 \text{K}$ . However, none of our models can reproduce the observed location of  $T_{\max}$ . While the location is observationally inferred to be between  $1.2R_{\odot}$  and  $1.6R_{\odot}$ , all of our models give  $r_{T_{\max}} < 1.2R_{\odot}$ . This is because the dissipation length of the N-waves is essentially short, even though one considers long period-waves that are generated in the corona. We can summarize that acoustic waves excited in the corona could certainly heat the surrounding plasma to  $T > 10^6 \text{K}$ , however, they cannot maintain the high temperature till the sufficiently distant region by themselves. Therefore, the cooperations with other heating sources with larger dissipation length are necessary to explain the observed solar corona.

### 3.3.3. Velocity Distribution

In fig.10, we show the results of velocity distribution of the solar wind, with observational results in the low-latitude streamer (shaded). The observational data are from Sheeley et al. (1997), who determined velocity profile between 2 and 30  $R_{\odot}$  from measurements of about 65 moving objects in the streamer belt. They used two different technic in deriving the results, whereas the shaded area displayed in fig.10 are based on the straight-line fit method (an upper panel of fig.6 in Sheeley et al. (1997); The shaded region is traced from that figure). Figure 10 indicates that the resultant velocity of our models is lower than the observed data in the whole region. The observation exhibits rapid acceleration in  $3 \sim 5R_{\odot}$ , while our results show gradual acceleration by thermal gas pressure, since the N-waves are damped in  $< 1.5R_{\odot}$  and wave pressure cannot contribute to the acceleration of the wind flow, as shown in figs.1 and 2. Other mechanisms are also required in acceleration of the low-speed wind.

## 4. Summary and Discussions

We have investigated the process of acoustic waves generated in the corona as a heating source especially in the mid- to low-latitude corona where the low-speed winds come from. We have found that the acoustic waves with  $\tau \geq 60\text{s}$  and  $F_{w,0} \geq 2 \times 10^5 \text{erg cm}^{-2}\text{s}^{-1}$  could certainly heat up the ambient plasma to  $T \geq 10^6\text{K}$  by the dissipation of the N-waves even in a flow tube with the areal expansion of  $f_{\text{max}} = 5$ , by balancing with the losses of the radiative cooling, the downward thermal conduction, and the adiabatic loss by the solar wind. Due to its dissipative character, the dissipation of N-waves effectively works in the inner corona and reproduces the density profile observed in the streamer region. However, it cannot contribute to the heating of the outer corona, since most of the wave energy is damped within a region of few-tenth of the solar radius even if one considers the waves with a long period of  $\tau = 300\text{s}$ . As a result, it is impossible to explain the observed temperature profile and flow velocity of the low-speed wind only by that process. Therefore, other mechanisms with the larger dissipation length should play a role cooperatively in the coronal heating and the acceleration of the low-speed wind.

Small-scale reconnection events and spicules also predict generation of fast shock waves (Lee & Wu 2000; Lee 2001; Hollweg 1982), though we have concentrated on the role of the N-waves (slow shocks along the magnetic field line) excited by those events in this paper. The dissipation length of the fast shocks must be larger than N-waves with the identical period, since their phase speed is  $\gtrsim v_A$ , which is much larger than that of the N-waves ( $\sim c_s$ ) for low- $\beta$  coronal plasma. Hence, cooperation with the fast shocks would give a more distant location of  $T_{\text{max}}$  to match the observed temperature profile (fig.9), and would let the

acceleration of the wind flow continue in the outer corona, as suggested by observation of the streamer belt (fig.10).

Finally, we had better remark an issue on anisotropic and selective heating of ions. According to recent observations (Strachan et al. 2002), O VI ions in the streamer have high perpendicular kinetic temperature, though this is not so extreme as that observed in the high-speed wind. Our results show that the deposition of energy and momentum from the N-waves to the ambient gas is completed in the region of  $r \lesssim 1.5R_{\odot}$ , where the particles are thermally well coupled. As a result, whatever anisotropies obtained by the N-wave heating would be wiped out and all the ions would have isotropic kinetic temperature. The process of the N-waves cannot explain the observed anisotropies, which also indicates that the other mechanisms causing the anisotropic heating have to operate simultaneously.

We thank K. Shibata, K. Ohki, K. Omukai, K. Tomisaka, H. Saio, S. Nitta, S. Inutsuka, T. Kudoh, Y. Yoshii, T. Kajino, and A. Tohsaki as well as members of DTAP in NAOJ for many valuable and critical comments and Y. Mclean for improvement of presentation in this paper. The author is supported by the JSPS Research Fellowship for Young Scientists, grant 5936.

## REFERENCES

- Allen, C. W. 1973, *Astrophysical Quantities*(London:Athlone)
- Aschwanden, M. J., Poland, A. I., & Rabin, D. M. 2001, *ARA&A*, 39, 175
- Bastian, T. S., Benz, A. O., & Gary, D. E. 1998, *ARA&A*, 36, 131
- Cranmer, S. R., Field, G. B., & Kohl, J. L. 1999, *ApJ*, 518, 937
- Erdélyi, R., Doyle, J. G., Perez, M. E., & Wilhelm, K. 1998, *A&A*, 337, 287
- Furusawa, K. & Sakai, J. I. 2000, *ApJ*, 540, 1156
- Habbal, S. R., Woo, R., Fineschi, S., O’neal, R., Kohl, J., Noci, G., & Korendyke, C. 1997, *ApJ*, 489, L103
- Hammer, R. 1982a, *ApJ*, 259, 767
- Hammer, R. 1982b, *ApJ*, 259, 779
- Hassler, D. M., Rottman, G. J., Shoub, E. C., & Holzer, T. E. 1990, *ApJ*, 348, L77

- Hayes, A. P., Vourlidas, A., & Howard, R. A. 2001, *ApJ*, 548, 1081
- Hollweg, J. V. 1982, *ApJ*, 254, 806
- Hollweg, J. V. 1992, *ApJ*, 389, 731
- Hollweg, J. V. 1999, *J. Geophys. Res.*, 104, 24781
- Hollweg, J. V., Jackson, S., & Galloway, D. 1982, *Sol.Phys.*, 75, 35
- Hudson, H. S. 1991, *Sol.Phys.*, 133, 357
- Kopp, R. A. & Orall, F. Q. 1976, *A&A*, 53,363
- Krucker, S. & Benz, A. O. 1998, *ApJ*, 501, L213
- Kudoh, T. & Shibata, K. 1999, *ApJ*, 514, 493
- Landau, L. D. & Lifshitz, E. M. 1959, 'Fluid Mechanics'
- Landini, M. & Monsignori-Fossi, B. C. 1990, *A&AS*, 82, 229
- Lee, L. C. & Wu, B. H. 2000, *ApJ*, 535, 1014
- Lee, L. C. 2001, *Space Sci. Rev.*, 95, 95
- McWhirter, R. W. P., Thonemann, P. C., & Wilson, R. 1975, *A&A*, 40, 63
- Mihalas, D. & Mihalas, B. W. 1984, 'Foundation of Radiation Hydrodynamics', Oxford University Press
- Nishio, M., Yaji, K., Kosugi, T., Nakajima, H., & Sakurai, T. 1997, *ApJ*, 489, 976
- Osterbrock, D. E. 1961, *ApJ*, 134, 347
- Parenti, S., Bromage, B. J. I., Poletto, G., Noci, G., Raymond, J. C., & Bromage, G. E. 2000, *A&A*, 363, 800
- Parker, E. N. 1958, *ApJ*, 128, 664
- Parnell, C. E. & Jupp, P. E. 2000, *ApJ*, 529, 554
- Raymond, J. C., Suleiman, R., Kohl, J. L., & Noci, G. 1998, *Space Sci. Rev.*, 85, 283
- Roald, C. B., Sturrock, P. A., & Wolfson, R. 2000, *ApJ*, 538, 960 (RSW)
- Rosner, R. & Vaiana, G. S. 1977, *ApJ*, 216, 141

- Rosner, R., Tucker, W. H., & Vaiana, G. S. 1978, *ApJ*, 220, 643
- Sakai, J.I., Kawata, T., Yoshida, K., Furusawa, K., & Cramer, N. F. 2000, *ApJ*, 537, 1063
- Sandbæk, Ø. & Leer, E. 1994, *ApJ*, 423, 500
- Sheeley, N. R. Jr. et al. 1997, *ApJ*, 484, 472
- Stein, R. F. & Schwartz, R. A. 1972, *ApJ*, 177, 807 (SS)
- Strachan, L, Suleiman, R., Panasyuk, A. V., Biesecker, D. A., & Kohl, J. L. 2002, *ApJ*, 571, 1008
- Sturrock, P. A. 1999, *ApJ*, 521, 451 (S99)
- Sturrock, P. A., Roald, C. B., & Wolfson, R. 1999, *ApJ*, 524, L75
- Tarbell, T., Ryutova, M., & Covington, J. 1999, *ApJ*, 514, L47
- Tsuneta, S. et al. 1992, *PASJ*, 44, L63
- Tsuneta, S. 1996, *ApJ*, 456, 840
- Ulmschneider, P. 1971, *A&A*, 12, 297
- Ulrich, R. K. 1996, *ApJ*, 465, 436
- Withbroe, G. L. & Noyes, R. W. 1977, *ARA&A*, 15, 363
- Withbroe, G. L. 1988, *ApJ*, 325, 442

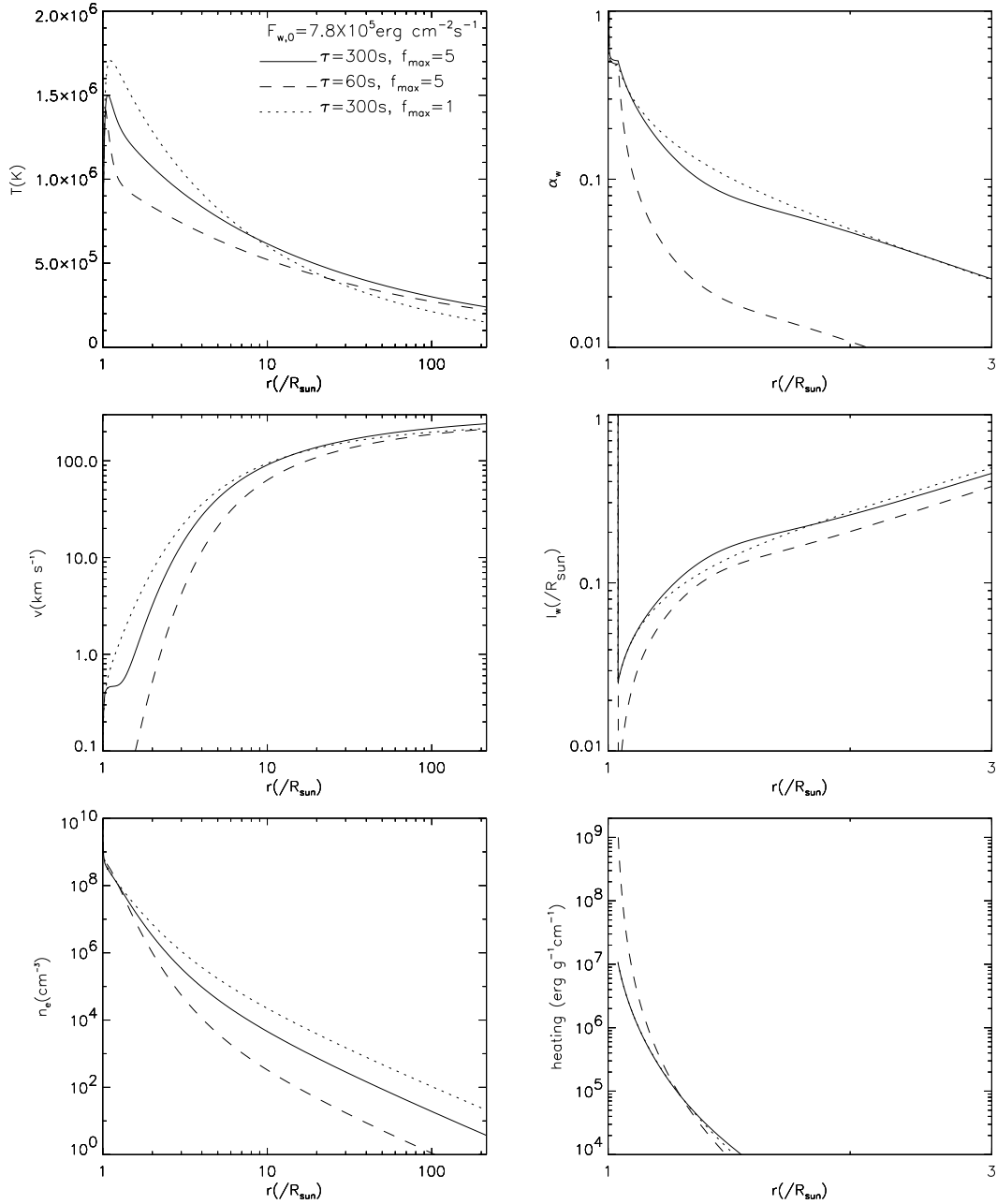


Fig. 1.— Variation of coronal wind structures on different sets of wave periods (in second) and the geometrical expansion factor,  $(\tau, f_{\text{max}}) = (300, 5)$  (solid),  $(60, 5)$  (dashed), and  $(300, 1)$  (dotted) for the same  $F_{w,0} = 7.8 \times 10^5 \text{ erg cm}^{-2} \text{ s}^{-1}$ . On the left, distributions of temperature, flow velocity, and density from the inner boundary to 1AU ( $= 215R_{\odot}$ ) are displayed from the top to the bottom. On the right, wave amplitude,  $\alpha_w$ , scaled by ambient sound velocity, Dissipation length,  $l_w$ , of the waves, and heating per mass from the inner boundary to  $3R_{\odot}$  are presented from the top to the bottom.

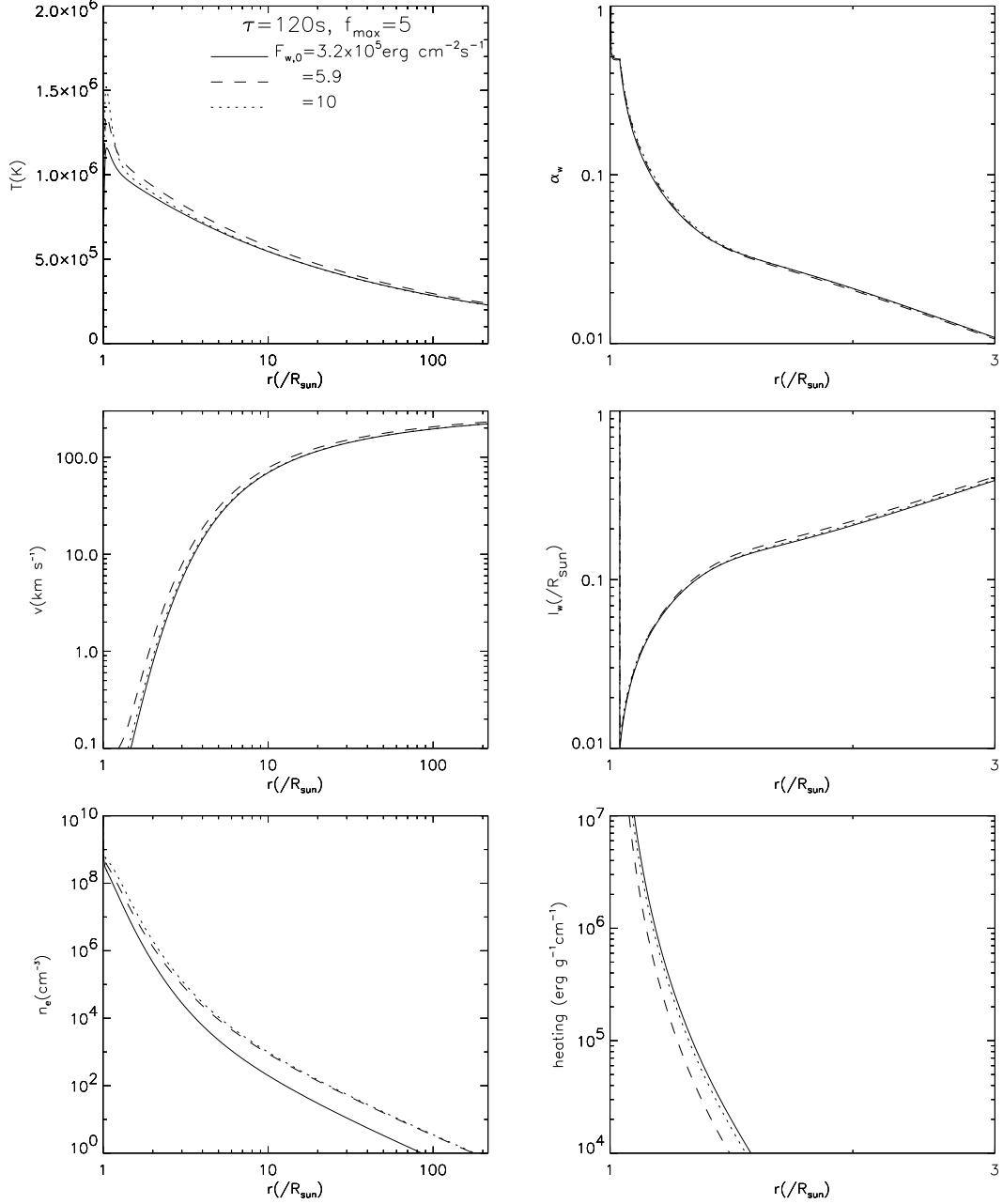


Fig. 2.— Variation of coronal wind structures on three different  $F_{w,0} = (3.2, 5.9, 10) \times 10^5$  erg cm $^{-2}$ s $^{-1}$  (solid, dashed, and dotted lines, respectively) for  $\tau = 120$  s and  $f_{\text{max}} = 5$ . Each panel is same as fig.1.



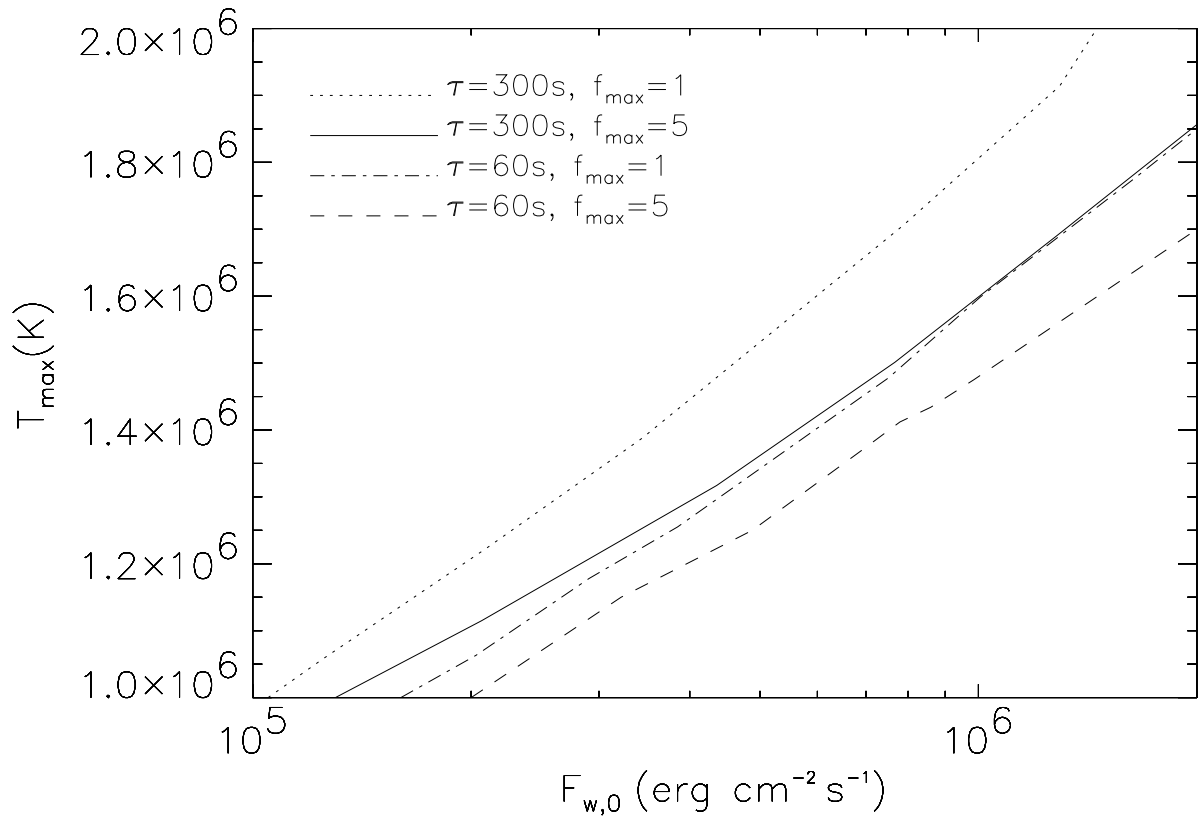


Fig. 3.— Relation between  $F_{w,0}$  and  $T_{\max}$  on different sets of  $(\tau, f_{\max})$ .

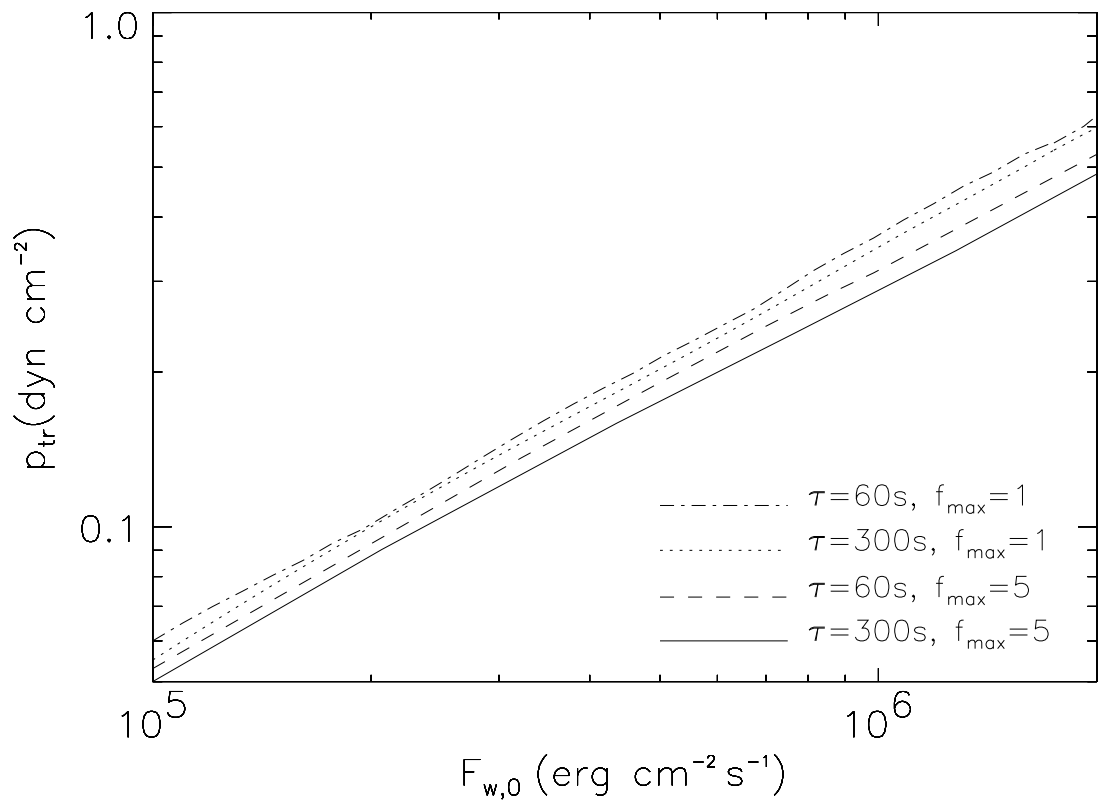


Fig. 4.— Relation between  $F_{w,0}$  and  $p_{\text{tr}}$  on different sets of  $(\tau, f_{\text{max}})$ .

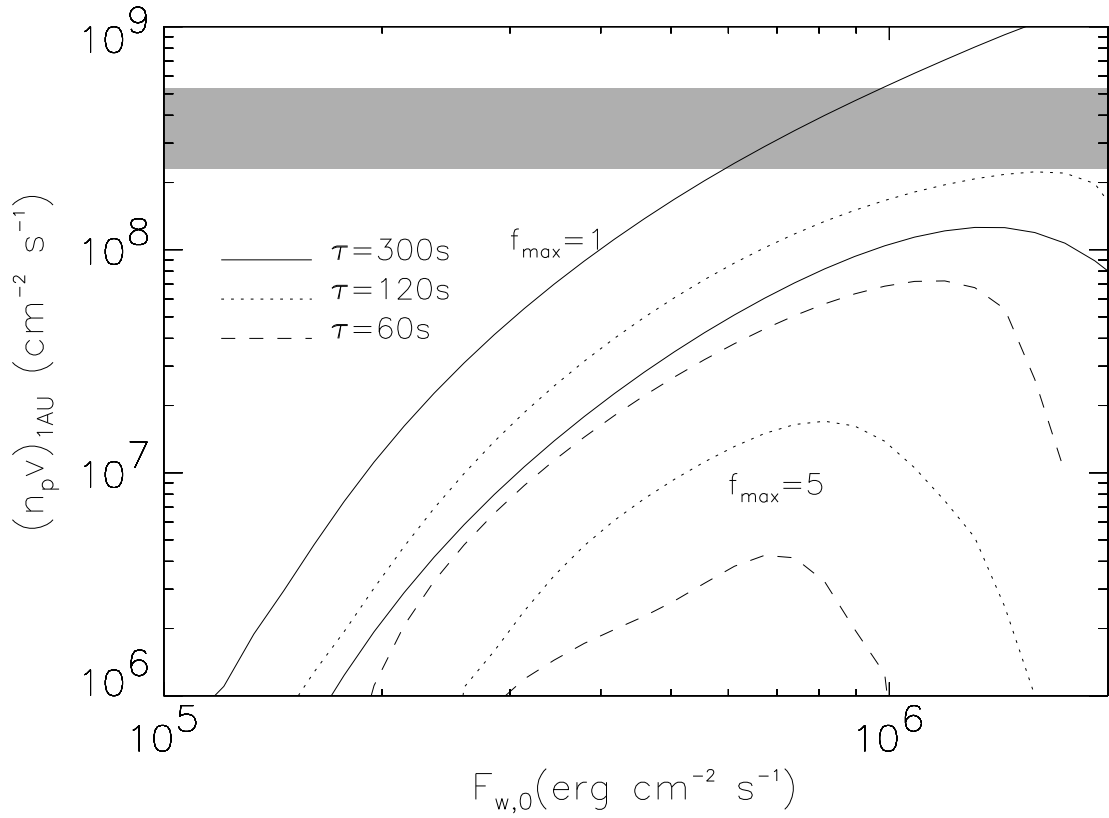


Fig. 5.— Relation between  $F_{w,0}$  and  $(n_p v)_{1AU}$  on  $f_{max} = 1$  and 5. Solid lines are results for cases adopting  $\tau = 300s$ , dotted lines, 120s, and dashed lines, 60s. Shaded region is the observational constraint by Withbroe (1988) for 'quiet corona'.

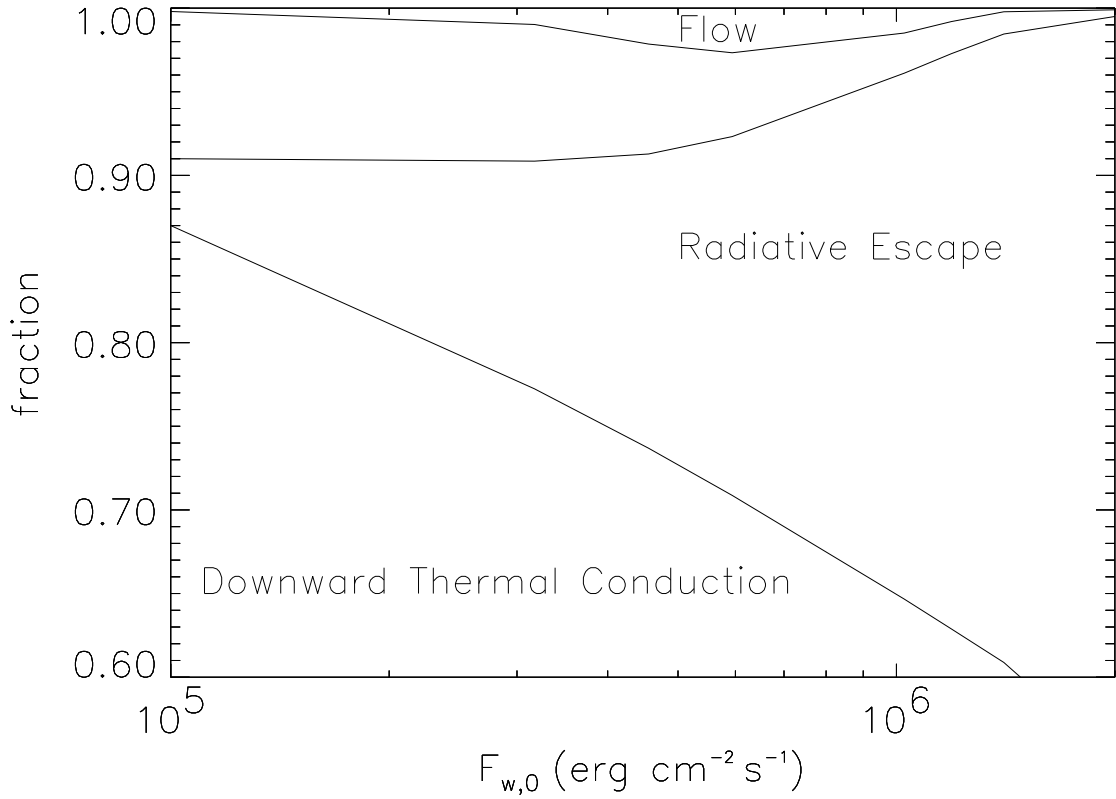


Fig. 6.— Fraction of three types of coronal energy loss, downward thermal conduction, radiative escape, and flow of the solar wind (mass loss), as a function of  $F_{w,0}$  for the  $\tau = 120$ s waves in the flow tube with  $f_{\max} = 5$ . The non-labeled region between 'radiative escape' and 'flow' indicates energy carried away to the outside of  $r_{\text{out}} = 300R_{\odot}$  by outward conduction.

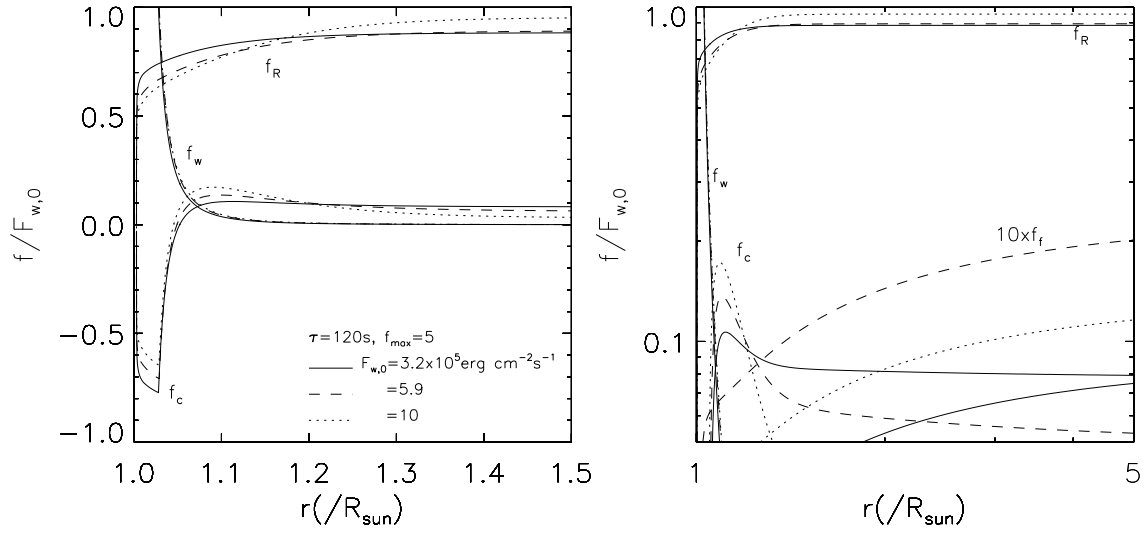


Fig. 7.— Exchange of energy among four components of energy flux, wave, radiation, conduction, and flow (consult text for detail). The 'flow' component is increased by 10 times. Models adopt the same inputs of  $\tau = 210\text{s}$  and  $f_{\text{max}} = 5$ , but different  $F_{w,0} = (3.2, 5.9, 10) \times 10^5 \text{ erg cm}^{-2} \text{ s}^{-1}$  (solid, dashed, and dotted lines, respectively)

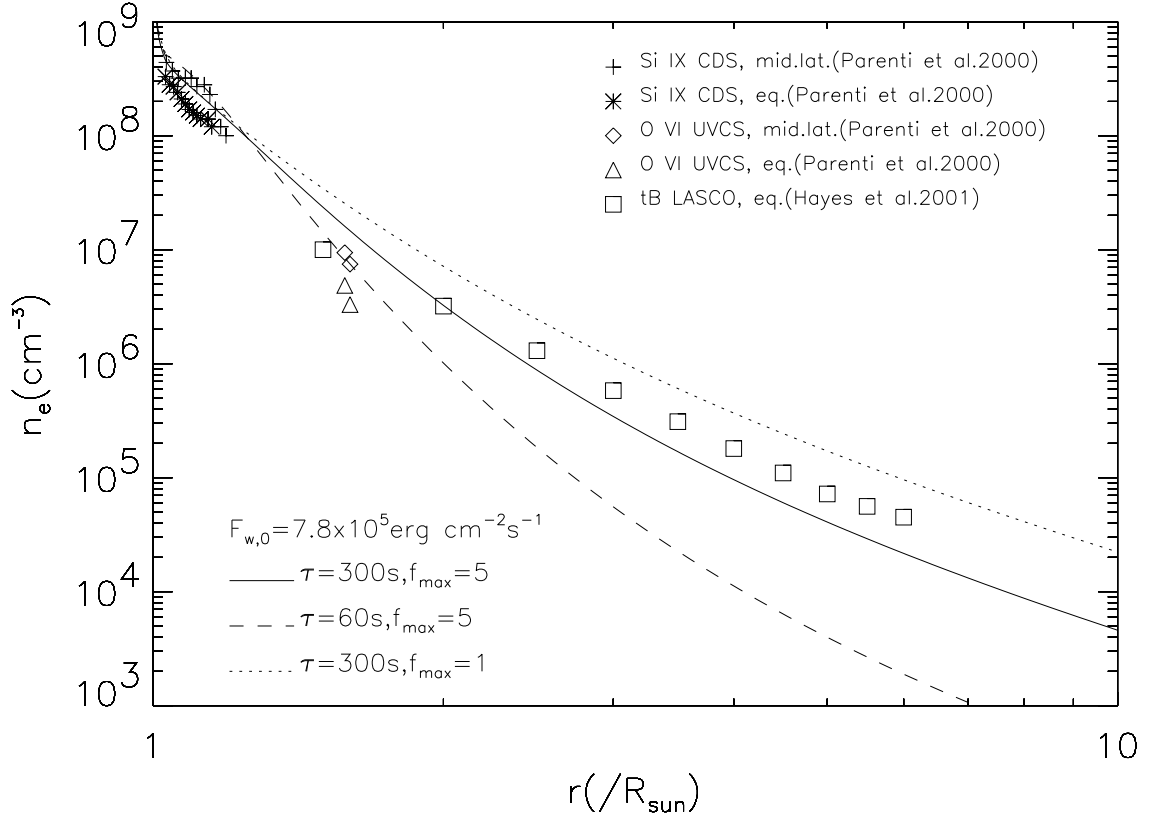


Fig. 8.— Comparison of electron density distributions. Lines are model results and points are observational data. Models adopt the same  $F_{w,0} = 7.8 \times 10^5 \text{ erg cm}^{-2} \text{ s}^{-1}$  and different sets of  $(\tau(\text{s}), f_{\text{max}}) = (300, 5)$  (solid),  $(60, 5)$  (dashed), and  $(300, 1)$  (dotted). Pluses are data from CDS/SOHO observation of the mid-latitude streamer, asterisks from CDS/SOHO observation of the equatorial streamer, diamonds from UVCS/SOHO observation of the mid-latitude streamer, and triangles from UVCS/SOHO observation of the equatorial streamer (Parenti et al. 2000). Squares are derived from observation of total brightness by LASCO/SOHO (Hayes, Vourlidas, & Howard 2001).

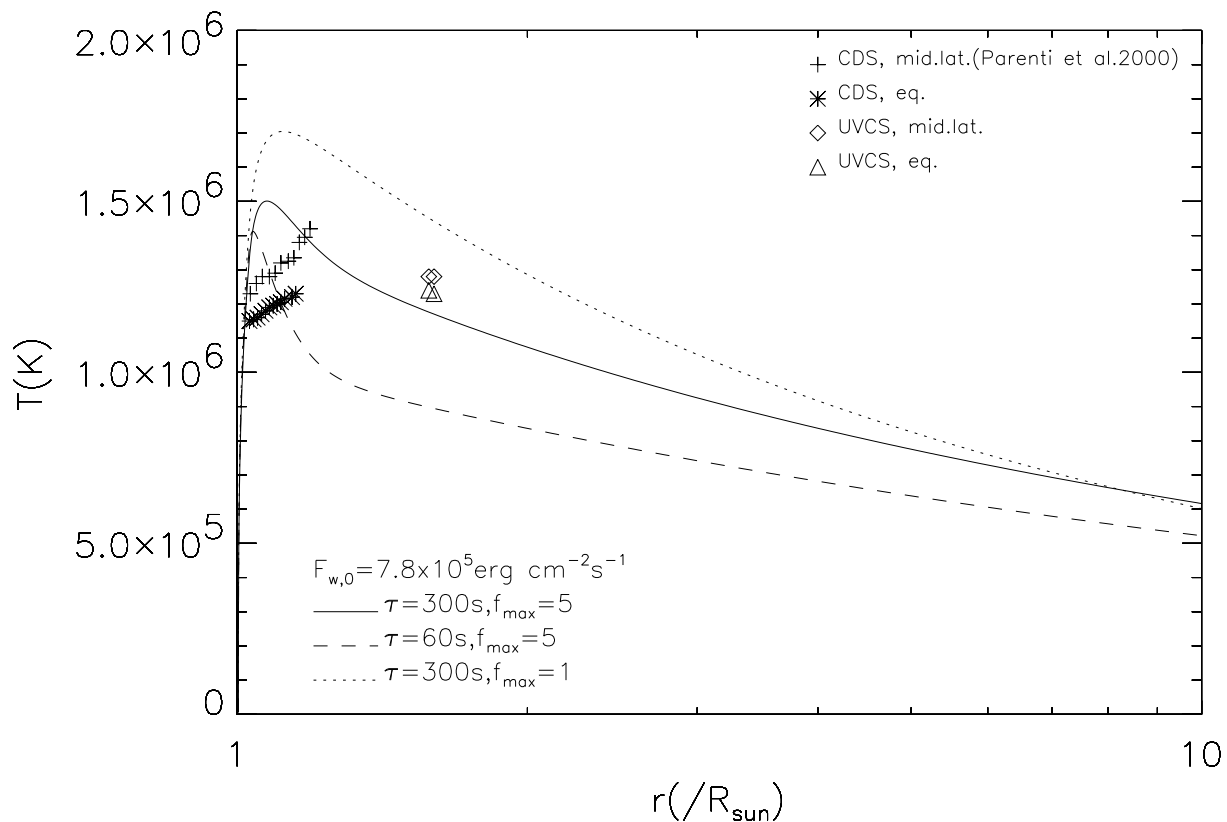


Fig. 9.— Comparison of electron density distributions. Respective lines represent results of the models adopting the same parameter sets as in fig.8. Pluses are data from CDS/SOHO observation of the mid-latitude streamer, asterisks from CDS/SOHO observation of the equatorial streamer, diamonds from UVCS/SOHO observation of the mid-latitude streamer, and triangles from UVCS/SOHO observation of the equatorial streamer (Parenti et al. 2000).

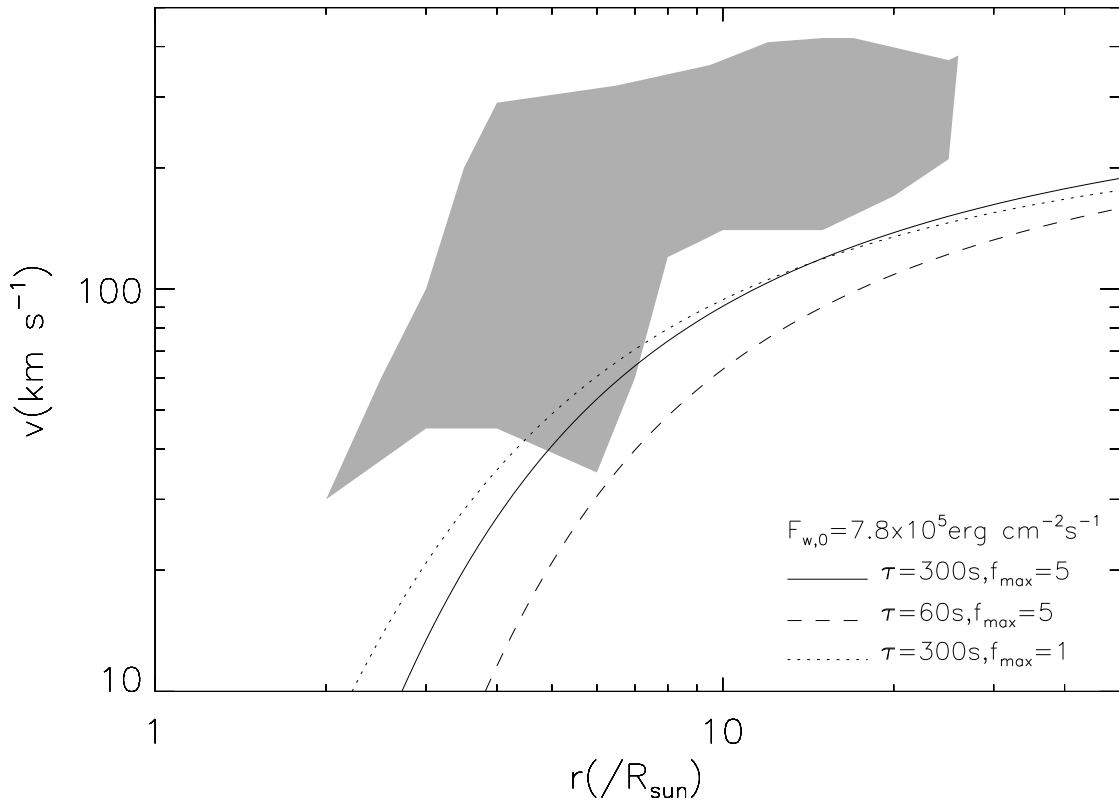


Fig. 10.— Comparison of velocity profile of the solar wind. Respective lines represent results of the models adopting the same parameter sets as in fig.8. Shaded region is observational data derived from measurements of about 65 moving objects in the streamer belt (Sheeley et al. 1997) (See text).